Landslide characterization using P- and S-wave seismic refraction tomography – the importance of elastic moduli

S. Uhlemann[a,b], S. Hagedorn[b], B. Dashwood[a], H. Maurer[b], D. Gunn[a], T. Dijkstra[a], J. Chambers[a]

[a] – British Geological Survey, Keyworth, Nottingham, UK, [b] – ETH Zurich, Institute of Geophysics, Zurich, Switzerland

Corresponding author: Sebastian Uhlemann, suhl@bgs.ac.uk

Abstract

In the broad spectrum of natural hazards, landslides in particular are capable of changing the landscape and causing significant human and economic losses. Detailed site investigations form an important component in the landslide risk mitigation and disaster risk reduction process. These investigations usually rely on surface observations, discrete sampling of the subsurface, and laboratory testing to examine properties that are deemed representative of entire slopes. Often this requires extensive interpolations and results in large uncertainties. To compliment and extend these approaches, we present a study from an active landslide in a Lias Group clay slope, North Yorkshire, UK, examining combined P- and S-wave seismic refraction tomography (SRT) as a means of providing subsurface volumetric imaging of geotechnical proxies.

The distributions of seismic wave velocities determined from SRT at the study site indicated zones with higher porosity and fissure density that are interpreted to represent the extent and depth of mass movements and weathered bedrock zones. Distinguishing the lithological units was facilitated by deriving the Poisson's ratio from the SRT data as saturated clay and partially saturated sandy silts showed distinctively different Poisson's ratios. Shear and Young's moduli derived from the SRT data revealed the weak nature of the materials in active parts of the landslide (i.e. 25 kPa and 100 kPa respectively). The SRT results are consistent with intrusive (i.e. cone penetration tests), laboratory, and additional geoelectrical data form this site. This study shows that SRT forms a cost-effective method that can significantly reduce uncertainties in the conceptual ground model of geotechnical and hydrological conditions that govern landslide dynamics.

Keywords

Seismic Refraction Tomography; Landslide characterization; Elastic Moduli; Site Investigation

1. Introduction

Landslides form one of the major natural hazards and accounted for at least 4600 fatalities per year between 2004 and 2010 (Petley, 2012). In addition there is significant economic impact, by affecting transport and utility infrastructure (Bird and Bommer, 2004; Dijkstra et al., 2014; Glendinning et al., 2014), and due to material loss which accounted for at least 1.7 billion US$ in the last century (Lacasse and Nadim, 2009; Nadim et al., 2013; Petley, 2013). Detailed investigations of slopes, which pose a risk to communities and infrastructure, are needed to reduce the uncertainty of the ground models (BSI, 2015). This involves characterisation (in space and in time) of the mechanical and hydrological conditions that define the stability of a slope (Leroueil, 2001). Determining the spatial distribution of parameters, such as soil thickness, weathering profile, and elastic material properties are crucial for landslide hazard and risk zonation (van Westen et al., 2006). Being able to provide a better defined ground model will lead to the design of more appropriate intervention, improved risk mitigation, and landslide disaster risk reduction strategies (Crozier and Glade, 2005; Popescu and Sasahara, 2009).

Geotechnical investigations, such as cone penetration tests and laboratory studies, are focussed on discrete points of a landslide, sampling a small volume of the material only. Landslides, due to their geomorphological characteristics, are complex structures, showing high variability in their physical properties (Cascini et al., 2015). Thus, geotechnical investigations, delivering "true" mechanical and hydrological properties, need to be supplemented by methods that allow for a definition of their spatial variability (Jongmans and Garambois, 2007; Perrone et al., 2014). Therefore, landslide studies frequently comprise geophysical measurements alongside geotechnical and laboratory characterization (Sass et al., 2008; Schrott and Sass, 2008; Gunn et al., 2013; Springman et al., 2013; Lissak et al., 2014; Salas-Romero et al., 2015). Out of the range of available geophysical techniques, electrical resistivity tomography (ERT) and seismic imaging methods are perhaps the most frequently applied to landslide studies (Jongmans and Garambois, 2007; Schrott and Sass, 2008; Van Dam, 2012; Perrone et al., 2014).

In a landslide characterization context, P-wave seismic refraction tomography is most commonly applied, as seismic velocities usually show significant differences between the landslide mass and the underlying bedrock (Heincke et al., 2006; Donohue et al., 2012; Yamakawa et al., 2012). However, for slopes that consist of similar sediments, a delineation of the different units and the effect of geomorphic processes is usually not possible as seismic velocities overlap (Schrott and Sass, 2008). This may be overcome by employing P- and S-wave SRT, as P- and S-waves are affected differently by changes in saturation, porosity, or elastic moduli (Gregory, 1976; Macari and Laureano, 1996; Mondol et al., 2007; Pasquet et al., 2015). Derivation of Poisson's ratio from a combined imaging of P- and S-wave velocities has recently been successful in detecting saturation characteristics of shallow aquifers (Grelle and Guadagno, 2009; Pasquet et al., 2015). However, most of these studies implement a sequential acquisition of P- and S-wave refraction data or a combination of refraction and surface wave methods (Grandjean et al., 2009; Hibert et al., 2012), which may introduce potential pitfalls due to different source and signal signatures, and offsets in the acquisition layout.

This study employs simultaneous P- and S-wave SRT to study the elastic properties of a shallow clayey landslide. From the SRT results, distributions of shear and Young's moduli, as well as Poisson's ratio are derived. As these parameters define the elastic properties of the slope material, the likely modes of deformation of the landslide can be defined (i.e. whether this is characterised by plastic, brittle or flow-type failure; what the likely position/shape of the main slip surface is; and, potentially, how strains are expected to develop in slopes). The outcome of this study highlights the benefit of deriving elastic moduli and Poisson's ratio to cost-effectively conduct a thorough investigation of the mechanical and hydrological conditions defining the landslide behaviour and provides insights into how spatial distributions of elastic properties can be used to reduce the uncertainty in the landslide ground model and improve characterisation of the landslide behaviour.

1.1 Study area

The studied landslide is located at Hollin Hill, a south-facing hillslope with a mean slope angle of about 14°. It is close to the town of Terrington, about 10 km west of Malton, North Yorkshire, UK (54°06'38'' N, 0°57'30'' W), set in the Howardian Hills, an escarpment running approximately NW-SE. It is underlain by four formations (Fig. 1c) of Lower and Middle Jurassic age comprising, in ascending order, Redcar Mudstone (RMF), Staithes Sandstone and Cleveland Ironstone Formation (SSF), Whitby Mudstone Formation (WMF), and Dogger Formation (DF). The DF is a limestone- and sandstone-dominated unit, which caps the hill and forms a potential perched aquifer above the WMF (Gunn et al., 2013). The thickness of the DF varies considerably over the region as an effect of the formation occupying hollows in the underlying WMF, and reaches a local maximum of 8 m to the north of the site. The WMF is composed of grey to dark-grey mudstone and siltstone, including scattered bands of calcareous and sideritic concretions. It has a thickness of about 25 m and shows a sharp boundary with the overlying DF. The WMF is the failing formation at site and in the surrounding area. The formations of the Upper Lias Group, and the WMF in particular, are known to cause slope instabilities throughout the UK, accounting for as much as 7.5 % of all UK landslides, with a density of 42 landslides per 100 km^2 outcrop (Hobbs et al., 2012). The SSF, which underlies the WMF, comprises ferruginous, micaceous siltstone with fine-grained sandstone and thin mudstone partings, and has a thickness of about 20 m. It is heavily bioturbated and shows locally occurring masses of siderite and pyrite (Gaunt et al., 1980). In the lower and middle part of the slope it is associated with relatively well-drained mixtures of clay, silt and fine sand. The lower boundary shows a gradational change to poorly-drained RMF, which comprises grey, silty, calcareous, and sideritic mudstone and thin shelly limestones (Chambers et al., 2011).

The bedrock succession shows a local dip of about 5° to the north (Merritt et al., 2013). It is overlain by a thin layer of head deposits, ranging from 0.2 to 1.3 m, which are characterised by gravelly, sandy, silty clay with occasional organic inclusions. It is formed of locally derived material (mainly from the DF), reworked by a combination of geomorphological processes, such as hillwash, slope failure, and soil creep (Chambers et al., 2011; Uhlemann et al., 2016).

Using the nomenclature of Cruden and Varnes (1996), the landslide can be defined as a very slow to slow moving composite multiple earth slide-earth flow, with maximum movement rates of up to 3.5 m/y observed in recent years (Uhlemann et al., 2016). Based on previously published data, different authors have developed and continuously improved the geomorphological understanding of this landslide (Chambers et al., 2011; Merritt et al., 2013; Uhlemann et al., 2016). The latest understanding is that the translation-dominant domain (WMF) is the main driver for mass movement processes on this slope. Substantial rainfall leads to additional loads, a rise in pore water pressures and a loss of effective stress in the near-surface leading to the (re-)activation of shear strains along (pre-existing) shear surfaces at critical depths of around 2 to 3 m. As material slides towards the boundary between WMF and SSF it encounters a thin drape of aeolian sands overlying the SSF that act as a toe drain and causes the slides to slow down and build up ridges along the slope. Further phases of deformation can lead to local breakthrough and rapid acceleration of flow/slide-like movement forming lobes towards the base of the slope. Thin sand lenses incorporated within the slide mass can act as preferential flow-paths potentially leading to local substantially elevated pore pressures (Uhlemann et al., 2016). The upper parts of the slope are retrograding as shallow rotational slides, triggered by the progressive loss of support along the local toe of the slopes through ongoing deformation in the translation-dominant domain. Thus, the landslide complex shows translational movements towards the WMF-SSF boundary, which evolves to slide/flow-like behaviour forming lobes towards to toe of the slope and drives rotational failure retrograding into the upper slopes (Fig. 1c). For more general explanations on the different landslide mechanisms the reader is referred to, e.g., Hungr et al. (2014).

The paleo-landscape in this area was affected by the water level dynamics of an ice-marginal lake (Lake Mowthorpe) during the last glaciation in the Pleistocene. This lake was formed due to landslides damming the gorge through which meltwater and surface-water runoff took place. As water level in the lake rose and a spill point at the eastern edge of the lake was reached (at Bulmer Beck, Fig. 1a), rapid incision occurred and this drained the lake (Chambers et al., 2011). This likely caused changes in effective stresses in the slopes and potential over-steepening, causing landslides that again blocked the drainage pathways and reinitiated the process. Thus, this area is characterized by repeated slope movements and therefore by highly heterogeneous and poorly compacted sediments, which are prone to landsliding.

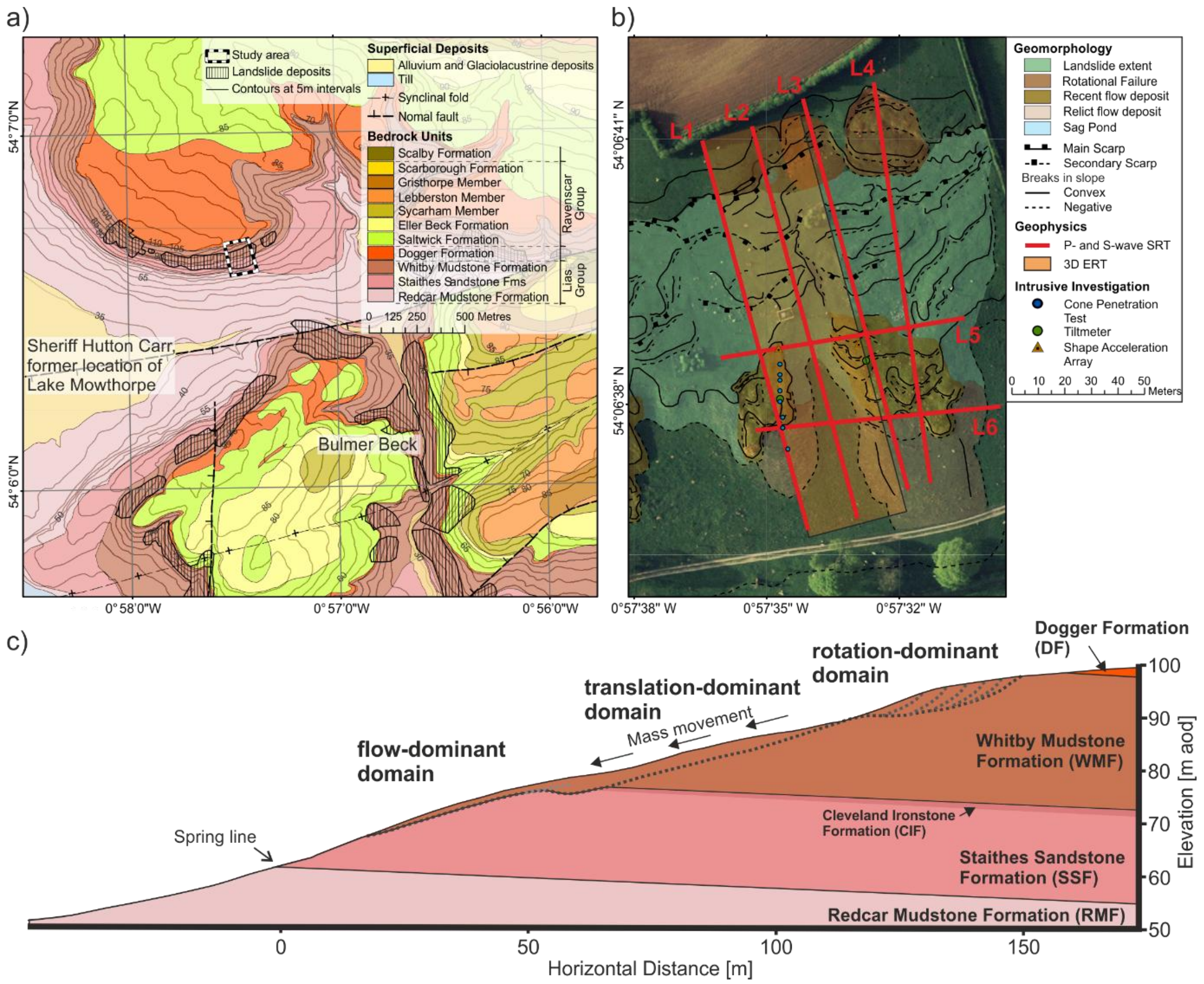

Fig. 1 a) Geological map of the study area. Note the high landslide occurrences that are constrained to the Whitby Mudstone Formation. b) SRT line locations superimposed on geomorphological map after Merritt et al. (2013) and aerial photograph. Also shown are the area of the 3D electrical resistivity tomography measurements and intrusive investigations. Aerial photograph © UKP/Getmapping License No. UKP2006/01. c) Ground-model of the study site, delineating the different landslide domains (modified after Gunn et al., 2013, and Uhlemann et al., 2016).

Hollin Hill is a well-studied landslide acting as a field laboratory to support UK landslide research. It is mainly focussed on technological developments in acoustic emission and electrical resistivity tomography, underpinning landslide monitoring and early warning (Wilkinson et al., 2010; Dixon et al., 2014; Smith et al., 2014; Smith and Dixon, 2015; Uhlemann et al., 2015; Wilkinson et al., 2016). Chambers et al. (2011) and Merritt et al. (2013) provide a thorough description of the landslide geology and geomorphology, which is mainly based on geoelectrical and borehole data, while Uhlemann et al. (2016) use long-term geotechnical monitoring data to derive an understanding of the geomorphological processes and triggering mechanisms controlling the landslide movements. This paper describes the result of a seismic characterization of the landslide, which can potentially aid in determining the elastic properties of the landslide material and thus may provide crucial input parameters for a physical modelling. It employs P-wave and S-wave seismic refraction tomography (SRT) with a specific focus to determine the spatial distribution of the elastic moduli of the landslide. To our knowledge, this is the first application of deriving elastic moduli from P- and S-wave SRT in a landslide context, and this paper will highlight its benefits to landslide research and characterization.

2. Methodology

2.1 Data acquisition

2.1.1 Survey parameters

The seismic survey consisted of six profiles, four of which (L1 to L4) extended from the toe to the top of the slope, and two (L5 and L6) were perpendicular to these. The perpendicular profiles covered the upper and lower part of two lobes (Fig. 1). While line L2 was located in a gully between two lobes, lines L1, L3, and L4 covered actively moving lobes, where L3 and L4 are located along the recently most active part of the landslide, showing movement rates of up to 3.5 m/year. Lines L1 to L3 were located adjacent to a permanently installed 3D electrical resistivity tomography (ERT) array, which also provided geoelectrical data during the SRT acquisition. Seismic data were acquired with a 2 m geophone and shot spacing, where shots were located between geophone locations (Fig. 2a). Each spread consisted of 48 three-component geophones with a natural frequency of 4.5 Hz, measuring vertical and two horizontal particle velocities. These were connected to six Geometrics® Geodes with 24 channels each. As each spread spanned over 94 m L1 to L4 were measured in two parts with an overlap of 32 and 26 m for L1 to L3, and L4, respectively. Each shot was recorded with a 0.5 ms sampling interval and a recording length of 1.5 s. These parameters were chosen based on test shots at site, which revealed very slow velocities that required long recording lengths. A 4.5 kg sledgehammer hitting a steel prism was used as seismic source. The prism was oriented perpendicular to the spread; for each side of the prism three recordings were acquired. The data acquisition of all six lines took 5 days and comprised a total number of 3156 shots. Each shot and geophone location was surveyed using RTK-GPS equipment.

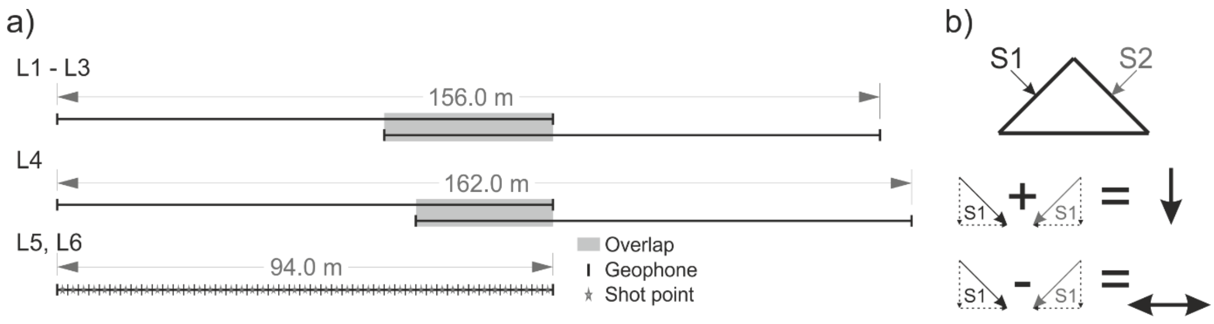

Fig. 2 a) Data acquisition layout. Note that the number of available channels and chosen geophone spacing of 2 m limited the maximum line length to 94 m. Thus, L1 to L4 comprise two spreads with 32 m and 26 m overlap for lines L1 to L3, and L4, respectively. The shot distribution applied on each line is shown on L5 and L6; shots were located with 2 m spacing between geophone locations. b) Source characteristics. A steel prism was hit from its two sides. Adding the two shots results in the vertical component of the wave field, while subtracting results in the horizontal component of the wave field.

2.1.2 Wave component extraction

By using a steel prism as seismic source P- and S-waves were excited at the same time. This reduced the acquisition time as only one source type was required, and also ensured the same source location and signature for both P- and S-wave SRT. This is in contrast to many other studies that are using distinct P- and SH-wave data acquisitions (e.g., Jongmans et al., 2009; Turesson, 2007). However, it required an additional processing step, as P- and S-wave source signatures had to be extracted. This was achieved by adding or subtracting the shots of the two different sides of the prism. Adding the two shots results in a “pure” P-wave source signature, that is, a vertically oriented force, and subtraction provides a “pure” S-wave source signature (Xia et al., 2002), that is, extraction of the horizontally oriented force (Fig. 2b). As the prism was oriented perpendicular to the geophone spread, only the horizontally polarized S-waves S_H will be analysed in following, assuming an isotropic S-wave propagation; S_H waves are referred to as S-waves hereafter. The addition and subtraction of shots of the two prism sides not only resulted in an extraction of the required wave field, but also mostly increased the Signal-to-Noise (S/N) ratio by an additional stacking (i.e. summation of two seismic traces). Note that inconsistencies between shots of different prism sides may result in a deteriorated the signal.

2.1.3 Data quality

The raw data quality was generally good to very good, despite the comparably high attenuation caused by the very soft material. The quality was further enhanced mainly by two procedures (1) data stacking of the three shots of each prism side, and (2) the additional stack as part of the wave field extraction. The initial stacking of shots from each prism side was guided by an analysis of the correlation coefficient ρ_{XY} of the two seismic traces X and Y, which is defined as:

$$\rho_{XY} = \frac{\sum_{i=1}^{N}(X_i - \bar{X})(Y_{i+\tau} - \bar{Y})}{\sigma_X \sigma_Y} \tag{1}$$

with the variance σ, the number of samples N, and a lag τ. If two traces show a correlation coefficient of ρ_{XY} = 1, the traces are identical. Correlation coefficients were calculated for each pair of the three shots, and a stacking threshold of ρ_{XY} > 0.85 was applied; traces were only kept if at least two of the three correlation coefficients were ρ_{XY} > 0.85. If, after this step, data acquired from each of the prism side was available, horizontal and vertical wave components were extracted, which implied a second stack. This requirement was fulfilled for more than 92 % of the data. These steps significantly improved the S/N ratio from an average of 2.79 dB to 6.97 dB, aiding the correct identification of the refracted waves (i.e. first arriving P- and S-waves, see Fig. 3).

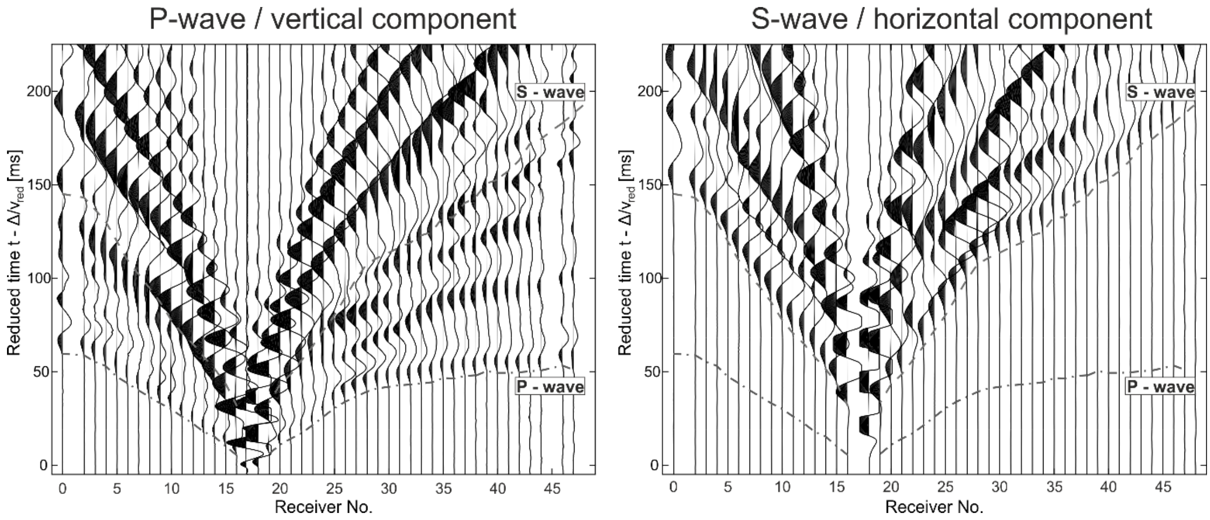

Fig. 3 Representative P- and S-wave shot gathers as generated after cross-correlation analysis, stacking, and wave-field extraction from the vertical and horizontal components, respectively. The two gathers show high S/N ratio, with first breaks clearly visible even at long offsets. Note that traces with low cross-correlation coefficients ($\rho_{XY} \leq 0.85$) were muted and gathers were reduced with a velocity of 3500 m/s.

2.2 Data analysis

2.2.1 First break picking

The recorded wave field (Fig. 3) includes surface, reflected, and refracted waves. For the purpose of this study we concentrate on the refracted waves, as these contain information about the subsurface velocity structure and thus the elastic moduli. This structure can be determined from the first-arrivals (or first-breaks) of the transmitted waves (see Fig. 3; for receivers 30 to 45 first arrivals can be found between 40 and 60 ms). These were determined from the shot gathers by manual and semi-automatic picking of the P- and S-wave first arrival for each of the 526 shots. A picking error of ±0.8 ms was determined from repeated picking of a subset of the data.

2.2.2 Inversion algorithm

The seismic P- and S-wave velocities of earth material can be defined in a simplified way as:

$$v_p = \sqrt{\frac{K + \frac{4}{3}G}{\rho}} \tag{2}$$

$$v_s = \sqrt{\frac{G}{\rho}} \tag{3}$$

where *K* is the bulk modulus, *G* the shear modulus, and *ρ* the density. *K* is defined as the ratio of hydrostatic stress to volumetric strain, and is a measure of a material's resistance to volume change under an applied stress. Similarly, the shear modulus is defined as the ratio of shear stress to shear strain (Mavko et al., 2009).

The methodology that was used to derive the subsurface velocity structure from the recorded travel times is described in detail in Lanz et al. (1998). In brief, tomographic images are derived from an algorithm that calculates the propagation of wave fronts through a 2-D heterogeneous medium and uses these results for an inversion to obtain the "true" subsurface velocity structures. The seismic problem can be simplified as a wave front traveling along the shortest ray-path in the time *t* from the source to the receiver *i* through a medium defined by its slowness (inverse of velocity) field *u*. If *u* is approximated by *k* cells with a constant slowness *u*, the forward problem can be formulated as (Lanz et al., 1998):

$$t = \sum_{k=1}^{m} G_{ik} u_k = \boldsymbol{G} u \tag{4}$$

with G_{ik} representing the respective cell travel time derivatives. From a given slowness field *u* travel times *t* can be calculated by determining ***G*** through minimization of the raypaths, using a finite-difference eikonal solver (Podvin and Lecomte, 1991). In the inverse problem, *u* is calculated from the determined first arrivals *t*. While in the case of the forward problem, the relationship between *t* and *u* is linear, in the inverse problem:

$$\boldsymbol{u} = \boldsymbol{G}^{-1} \boldsymbol{t}\,, \tag{5}$$

due to the dependency of ***G*** on ***u***, it is strongly non-linear and has to be solved iteratively. The inversion was performed separately for the P- and S-wave data.

2.2.3 Regularization

Additional constraints are needed to determine $\boldsymbol{u}$ from the seismic refraction data set, and are provided by the regularization parameters α and D_s. Including these parameters and error weights into the normal equation leads to the following notation of the inverse problem:

$$u_{est} = \left(\boldsymbol{G}^T \boldsymbol{W}_d^T \boldsymbol{W}_d \boldsymbol{G} + \alpha^2 \boldsymbol{I} + \boldsymbol{D}_s^T \boldsymbol{D}_s\right)^{-1} \boldsymbol{G}^T \boldsymbol{W}_d^T \boldsymbol{W}_d \, d_{obs} \, \alpha^2 \boldsymbol{I} \, u_{ref} \quad (6)$$

with the weighting matrix $\boldsymbol{W}_d$ containing the data errors, the identity matrix $\boldsymbol{I}$, and the reference slowness field u_{ref}. The parameter α defines how much deviations from a starting model are penalized (i.e. damps the inversion), while D_s minimizes the roughness of the model (i.e. enforces model smoothness).

The starting model was chosen based on the guidelines given in Lanz et al. (1998). For the P-wave inversion a starting model with a surface velocity of 500 m/s and a velocity gradient of 40 (m/s)/m was chosen, with a maximum velocity of 2500 m/s, which represents a typical value for poorly consolidated sandstone (Telford et al., 1990). The S-wave starting model comprised a surface velocity of 100 m/s, a velocity gradient of 20 (m/s)/m, and a maximum velocity of 1500 m/s, representative of saturated clays (Mondol et al., 2007). Note that the defined maximum velocities are likely to overestimate the conditions of the study site, thereby ensuring sufficient ray coverage for the inversion (Lanz et al., 1998). For both P- and S-wave tomography the model was discretized in the same way, having initial cell sizes at the surface of 2.0 m and 0.5 m in horizontal and vertical direction, respectively. As ray coverage decreases with depth, cell sizes are slightly increased. A maximum model depth of 60 m was defined for profiles L1 to L4, and 35 m for profiles L5 and L6.

The regularization parameters α and D_s were chosen based on inverting a wide variety of combinations of these parameters. Their magnitude controls the overall amount of regularization; if the parameters are too small the inversion becomes unstable and no solution can be found, while if they are too large the resulting tomogram will be overly smooth and/or show little deviation from the starting model (Fig. 4). After this test, the regularization parameters applied to all lines were chosen as α = 8 and D_s = 14; thus giving more weight to a smooth model than to a deviation from the starting model. The remaining root-mean-square (RMS) error between modelled and measured data ranged between 1.7 ms – 3.2 ms (for L2 and L6) for the P-wave travel time inversion, and between 3.4 ms – 6.7 ms (L2 and L6) for the S-wave travel time inversion, and are slightly larger than the picking error.

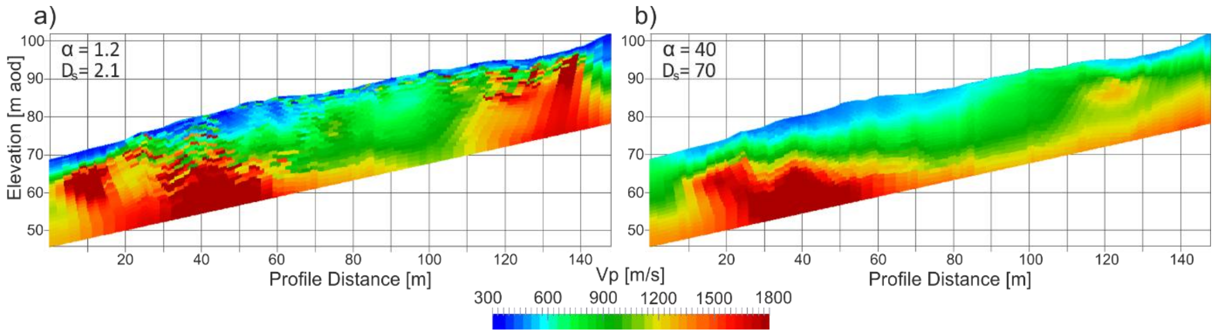

Fig. 4 Data of Line 3 inverted using (a) small magnitude of regularization (α = 1.2, D_s = 2.1) and (b) large magnitude of regularization (α = 40, D_s = 70). The ratio between smoothing and damping has been kept constant. Note that a small amount of regularization results in larger small scale v_p variation, while a large amount of regularization leads to reduced resolution and an overly smooth image of the subsurface velocity distribution.

3. Results

3.1 P-wave and S-wave tomography

The inverted P- and S-wave velocity models show generally very low to low velocities, with values ranging from 300 m/s to 1800 m/s, and 120 m/s to 600 m/s, respectively (Fig. 5). The smallest velocities in the P-wave tomograms (v_p < 500 m/s) are found less than 5 m below ground level (bgl) in the flow- and rotation-dominant domains of the landslide. In these domains, a sub-horizontal boundary can be found (dashed line in Fig. 5a), which in the flow-dominant domain increases in depth from about 5 m to 15 m bgl with increasing profile distance. At this boundary velocities increase rapidly from v_p < 500 m/s to v_p > 1600 m/s. This rapid increase is most pronounced at the flow-dominant domain, and is a consistent feature in all acquired profiles (Fig. 5c). Similar velocity gradients can be observed in the rotation-dominant domain of Line 3, but in the other profiles they are smaller and the feature less pronounced. Common to all P-wave tomograms is a deep-reaching low velocity anomaly between y = 65 m to 110 m, thus characterising the translation-dominant domain. While shallow velocities (< 5 m bgl) are higher than in the neighbouring domains, the velocity gradients are much smaller, and thus a rapidly increasing velocity with depth is missing; velocities remain below 1000 m/s up to a depth of 25 m bgl.

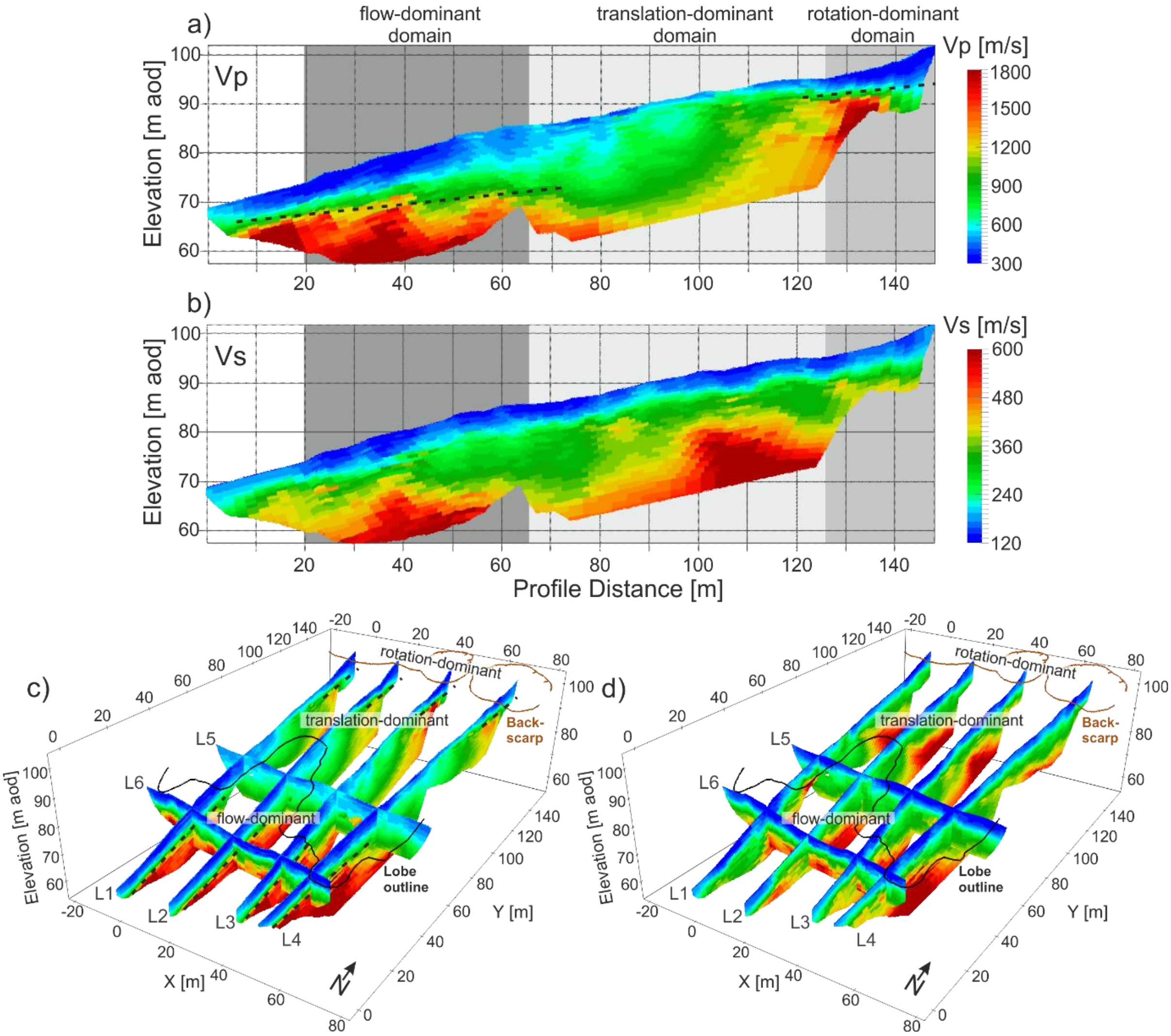

Fig. 5 a)-b) Images of P- and S-wave velocity distribution obtained from refraction data of Line 3. c)-d) 3D representation of all profiles (cross-sections of profiles L1, L2, and L4 to L6 can be found in the supplementary material). Highlighted are also domains of different movement characteristics (Gunn et al., 2013). *Note that the lowest P- and S-wave velocities are within the lobes of the flow-dominated area of the landslides. Shown are only the parts of the tomograms with ray coverage of both P- and S-waves, and investigation depths < 25 m.*

The S-wave tomograms show no differences in the velocities of the shallow parts (< 5 m bgl) of the translation-dominant domain compared to neighbouring flow- and rotation-dominant domains. However, the lowest velocities (v_s < 150 m/s) are observed above 5 m bgl in the flow-dominant domain. The lines of the eastern part of the landslide (Line 3 and 4) show a continuous shallow low-velocity layer, while this thins out over the translation-dominated domain of the western part. A significant increase in shallow velocities can be found just below the lobe (profile distance < 20 m, Fig. 5b). This is a consistent feature of all profiles covering the lobes (Lines 1, 3, and 4). These lines show significantly lower velocities in the flow-dominated domain than can be observed in Line 2, which is located between two lobes. This can also be observed in the crosslines, Line 5 and 6, which show higher velocities in this region (15 m < x < 25 m). The sharp boundary observed in the P-wave velocity tomograms is less well-developed in the S-wave velocity sections, appearing slightly deeper and with smaller velocity gradients. Similarly, a deep low S-wave velocity anomaly can be found in all profiles, which is less distinctive than in the P-wave velocity profiles. There is also good spatial consistency of the observed features in both the P- and S-wave velocity tomograms (Fig. 5c and d).

3.2 Elastic moduli

The most commonly used moduli to characterize soils are the small-strain shear modulus G_0 and Young's modulus E (either expressed in terms of undrained/total stress or drained/effective stress conditions). Both moduli provide a measure of the materials stiffness and are defined as ratio of stress to resulting strain along an axis resulting from shear (G) or loading (Young's E; Mavko et al., 2009; Clayton, 2011). G_0 is commonly defined as the ratio of shear stress to shear strain (γ_s) for very small strains ($\gamma_s < 1 \times 10^{-3}$; e.g. Atkinson, 2000; Benz, 2007). Guadalupe et al. (2013) describe that G_0 of soils shows a linear relationship with the effective stresses at failure for dilatant soils, independent of density, degree of cementation and confining stress. Both, G_0 and E, are frequently used in the estimation of soil consolidation (Biot, 1941; Das, 2008) and deformation analysis (Paice et al., 1996; Giannakopoulos and Suresh, 1997; Clayton, 2011), as well as physical landslide modelling (e.g., Lacroix and Amitrano, 2013). They are related through the Poisson's ratio *v*:

$$G = \frac{E}{2(1+\nu)} \tag{7}$$

For the purpose of seismic wave analyses both moduli are considered in terms of total stress conditions.

Equations 2 and 3 show that v_p and v_s are defined by the density and elastic moduli of the material that the waves are travelling through. Hence, if the distributions of seismic wave velocities and density are known, elastic moduli can be calculated, with the shear and Young's modulus being defined as:

$$G_0 = \rho {v_s}^2 \tag{8}$$

$$E = \frac{\rho {v_s}^2 (3{v_p}^2 - 4{v_s}^2)}{({v_p}^2 - {v_s}^2)} \tag{9}$$

A density model (Figure 6a) was estimated based on laboratory analysis of samples taken from site and by considering observed trends. The SSF was assigned a density of 2.05 Mg/m^3, while for the WMF and RMF a depth-varying density was assigned, increasing from 1.7 Mg/m^3 at the surface to 2.0 Mg/m^3 at about 15 m depth. These values were determined from site samples and informed by characteristic values (Hobbs et al., 2012). This simplification is justified as shear and Young's modulus show a linear dependence on the density, but quadratic to v_s. Thus the high sensitivity of the elastic moduli to variations of v_s outweighs potential inaccuracies of the density model, which is considered to be accurate to about 15 % of the true values.

As for v_p and v_s, the elastic moduli show low to very low values across the imaged landslide domains. Fig. 6a shows the distribution of the shear modulus along Line 3, which spans across the recently most active part of the landslide. The imaged features are comparable to the ones of the S-wave velocity distribution. Very low shear moduli (G_0 < 100 kPa) are generally found at depths of less than

5 m bgl, with the lowest values located in the shallow, actively moving parts of the landslide (profile distance > 20 m). The layer reaches its greatest thickness of up to 8 m in the upper part of the flow-dominant domain. This is a feature that is observed in all lines covering actively moving parts (Fig. 6c). Values increase to more than 200 kPa below 5 m, with G_0 reaching maxima of about 1 MPa. At a depth of about 20 m bgl, anomalies of higher shear moduli (>1 MPa) can be found below the flow-dominant domain (20 m < y < 60 m) and the upper part of the translation-dominant domain (100 m < y < 120 m). Young's modulus (Fig. 6b) shows a much thinner, shallow layer of E < 150 kPa, which reaches down to about 2 m bgl only. This layer is thinnest in the most stable areas of the landslide (line L2, Fig. 6d). Below this depth, Young's modulus rapidly increases to values of more than 1 MPa in about 10 m depth. An anomaly with slightly lower E can be found below the boundary between flow- and translation-dominant domains, with values of less than 500 kPa down to a depth of more than 20 m.

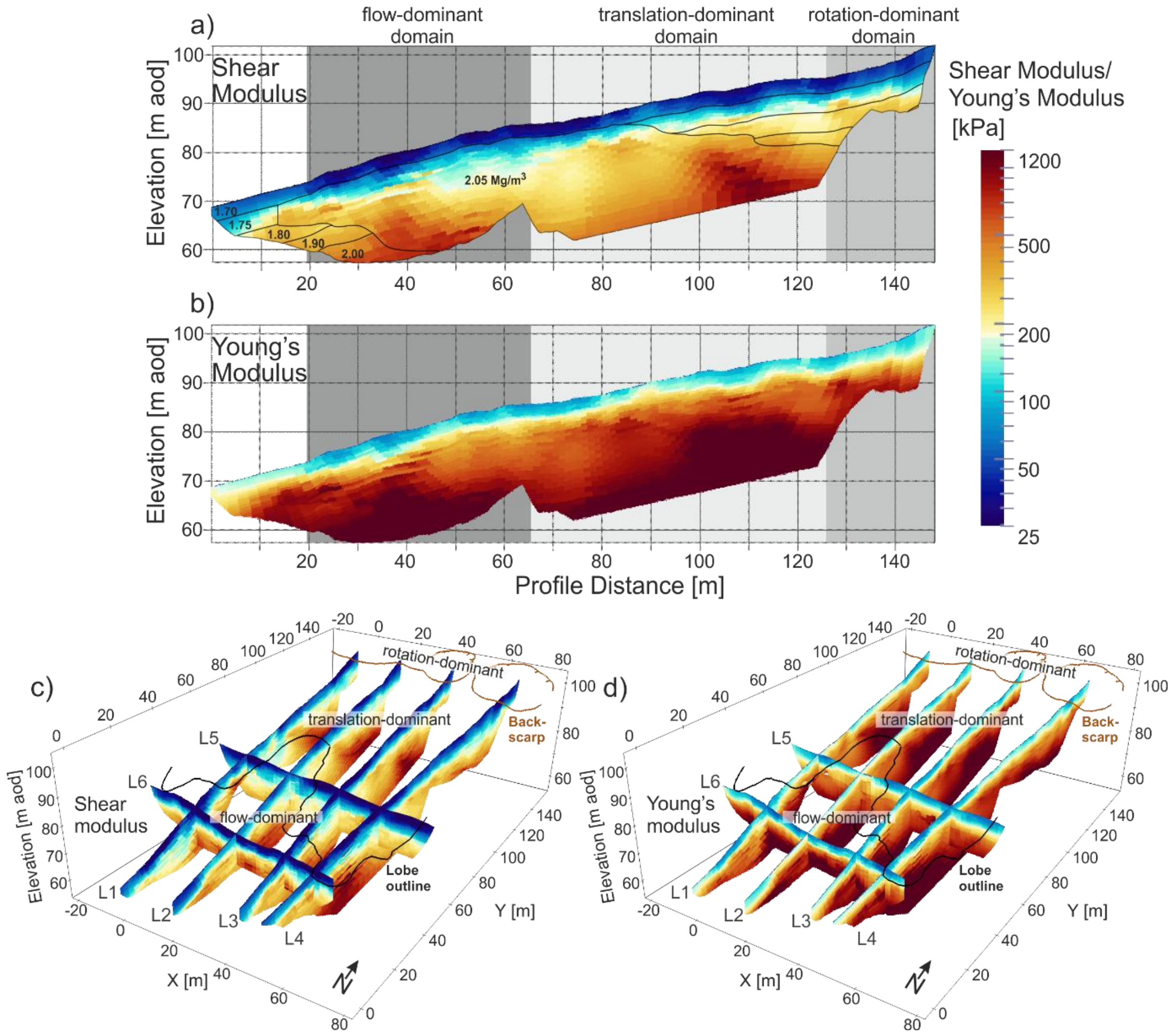

Fig. 6 Shear and Young's modulus. a)-b) Profiles of line L3, c)-d) 3D representation of all survey lines (cross-sections of profiles L1, L2, and L4 to L6 can be found in the supplementary material). The density model (in Mg/m^3) used in the calculation of the moduli is shown in a). Note that both shear and Young's modulus are plotted on the same colour scale. The location of the penetrometer test profile (P-P') is indicated in d). Shown are only the parts of the tomograms with ray coverage of both P- and S-waves, and investigation depths < 25 m.

3.3 Poisson's ratio

Another commonly used parameter in slope stability analysis is the Poisson's ratio *v* (e.g., Griffiths and Lane, 1999; Martel and Muller, 2000), which is strongly linked to the stress field in slopes and the degree of saturation of soil materials (Huang et al., 2012). It can be derived directly from the inverted v_p and v_s distributions by (Mavko et al., 2009):

$$\nu = \frac{{v_p}^2 - 2{v_s}^2}{2\left({v_p}^2 - {v_s}^2\right)}. \tag{10}$$

In contrast to the shear and Young's modulus, no density estimation is needed for the calculation of ν, highlighting the benefit of considering the Poisson's ratio by eliminating potential uncertainties rising from an assumed density model.

The Poisson's ratio is usually positive and ranges between 0 and 0.5, where 0.5 is characteristic for an incompressible fluid. For earth materials, ν approaching 0.5 is characteristic for fully saturated clays, while partially saturated silt or sandy clays show lower values between 0.2 and 0.4 (Davidovici, 1985; Bowles, 1988).

The Poisson's ratio profiles show spatially consistent features, delineating sub-horizontal, distinct layers separated by ν values of approximately 0.4 (Fig. 7). Throughout the survey area ν shows a minimum of about 0.08 and a maximum of 0.49. The shallow subsurface of the translation-dominant domain is characterized by very high Poisson's ratios of $\nu > 0.40$, which reach deeper levels (down to about 25 m bgl) towards the northern boundary of the study area. This is also evident in profile L3, at profile distances between 100 m and 140 m; approaching the northern boundary, this layer of high Poisson's ratio is overlain by a material with lower ν. Note also that this layer, at its lower boundary (at a profile distance between 50 m and 95 m) thins out and reaches the flow-dominant domain. This is only evident on profiles covering lobes (L1, L3, and L4). Beneath, and extending to the surface at the lower part of the flow-dominant domain (profile distance of 10 m to 50 m), significantly lower values of ν are found, ranging between 0.08 and 0.40. These values represent a layer with a thickness ranging between 5 m and 20 m. In the shallow parts of the landslide complex, this layer is most clearly distinguishable at L2, which is located between two lobes, without accumulation of flow deposits. Below it, ν increases again to values reaching 0.49.

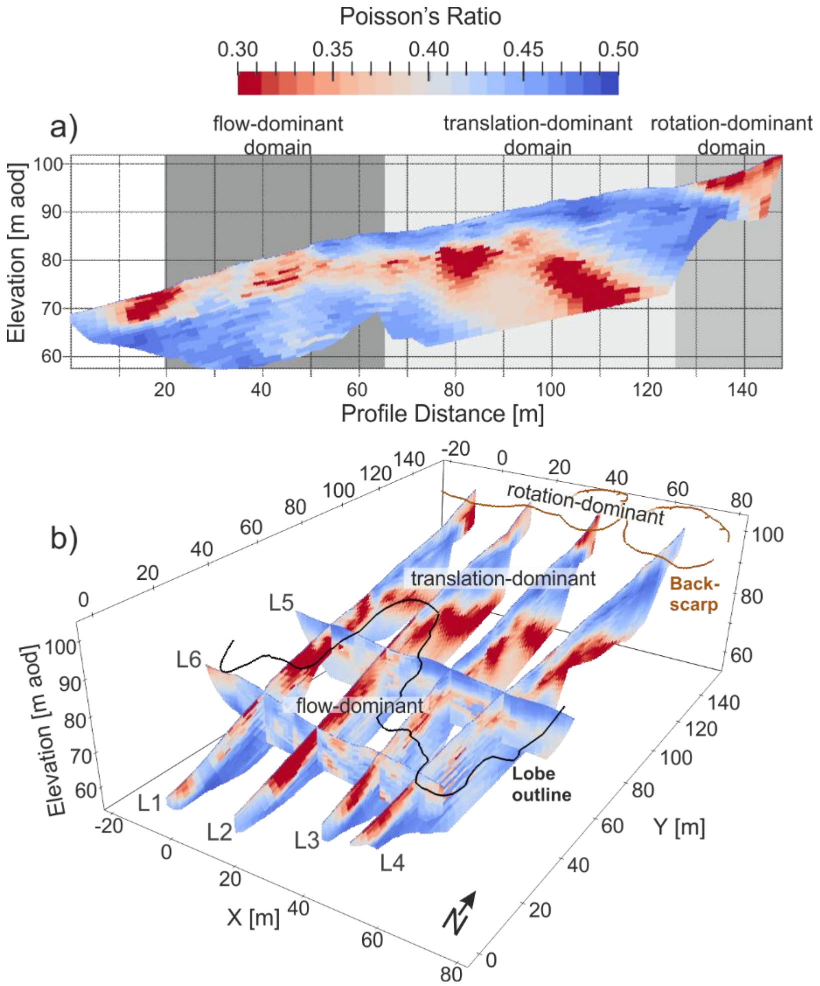

Fig. 7 Poisson's ratio of (a) profile L3, and (b) all profiles (cross-sections of profiles L1, L2, and L4 to L6 can be found in the supplementary material). Note the smaller values in the central part of the landslide. This area coincides with the previously known location of the SSF. Shown are only the parts of the tomograms with ray coverage of both P- and S-waves, and investigation depths < 25 m.

4. Discussion

4.1 P- and S-wave tomography

P- and S-wave SRT was employed to delineate the thickness of the WMF deposits, as the WMF was expected to show lower seismic velocities than the SSF. This assumption was mainly based on expected differences in bulk density and elastic moduli; while the material of WMF can be classified as clay (Schaetzl and Anderson, 2005) with a bulk density expected to be about 1.7 Mg m^{-3}, the SSF is usually classified as a sandy clay to sandy clayey silt, with bulk densities exceeding 2.0 Mg m^{-3}.

However, neither P- nor S-wave velocity tomograms showed distinct velocities in areas known to represent WMF and SSF (Fig. 1c). While shear wave velocities of less than 280 m/s are characteristic for clay soils, soils of fine to coarse sand can show v_s values ranging between 70 and 800 m/s (Ohta and Goto, 1978). Due to these overlapping ranges it was not possible to differentiate between WMF and SSF solely from the S-wave SRT. Throughout the study area, weathering and destressing has weakened these sedimentary lithologies to an extent that shear wave velocities are v_s < 700 m/s above 20 m bgl (Yilmaz (2015) defines v_s = 700 m/s as a threshold to define 'geotechnical bedrock').

Hobbs et al. (2012) note that the bulk density of the WMF is likely to be reduced by periglacial frost action, weathering and de-stressing in the near surface, affecting the material down to a depth of about 10 m. In turn this will lead to a reduction in the shear modulus (e.g. Macari and Laureano, 1996) and, in conjunction with a high fissure density, causes the very low P- and S-wave velocities observed in the upper 5 m bgl. Weathering usually decreases with increasing depth, and thus higher P- and S-wave velocities are observed at deeper layers (Yamakawa et al., 2012).

P-wave velocities of about 800 m/s can be regarded as a critical stiffness threshold (CST) separating 'geotechnical bedrock' (in the sense of Yilmaz, 2015) from weathered/deconstructed materials above. The depth at which this threshold is manifested at Hollin Hill is usually found between 5 m and 12 m bgl. Above this depth, the lowest P-wave velocities are found, with minima being located in the flow and translation dominated domains where materials are characterised by advanced de-structuring and significantly increased porosities as a consequence of progressive straining and reworking. The reduction of v_p with increasing porosity is higher for saturated material (Caris and Van Asch, 1991; Mondol et al., 2007). This correlates with field observations where fully saturated materials in the translations dominant domain are denser and thus have higher Poisson ratios in comparison to the lower density flow deposits that deform more readily. The low values observed in the backscarp area are generally due to partially saturated materials at the near surface during the time of investigation. Comparing the laboratory results of Mondol et al. (2007) to the inverted P- and S-wave velocities suggest that near-surface material may show porosities of up to 70 %.

While S-waves show only a limited response to changes in moisture content, P-wave velocities are known to show a significant increase with increasing moisture content (Gregory, 1976). Thus the high P-wave velocity anomaly (v_p > 1500 m/s), consistently found at depths between 5 m and 20 m bgl in the lower part of the slope (y < 60 m) is likely to indicate the regional groundwater level (Turesson, 2007). Extrapolating this boundary outside the study area coincides with the location of a spring line below the toe of the slope. The DF at the northern-most part of the study area is known to show a perched water table; increased v_p are likely to be caused by the elevated moisture content in this area as well. Note that perched water tables are also found in the WMF and in the near-surface materials of the flow lobes, particularly following prolonged or intense rainfall.

The study area is known to have been affected by paleo-landsliding (Chambers et al., 2011; Merritt et al., 2013; Uhlemann et al., 2016). Thus the low-velocity anomaly in both v_p and v_s in the middle part of the slope could reflect a potential paleo-landslide, leading to the formation of the relict landslide deposits in the lower part of the slope (Merritt et al., 2013). However, the large lateral extent and the abundance of this feature in the elastic moduli and Poisson's ratio are more likely to suggest a lithological control (or increased weathering depth/extent). It is speculated that depth of penetration of periglacial processes is greater where WMF is not covered by surface deposits in the form of aeolian sands that have been found to cover the lower slopes (Uhlemann et al., 2016).

While the imaged P- and S-wave velocities do not provide much information about the extent of the lithological units, it is possible to gain a clear indication of the depth to which weathering affects the material, and, especially from v_p observations, provide an indication of the regional groundwater table.

4.2 Elastic moduli

Similarly to the P- and S-wave velocities, shear and Young's modulus are reduced by weathering processes (Macari and Laureano, 1996). The low values of the moduli in depths < 5 m bgl can therefore be attributed to soil weathering and reworking through mass movements. In these shallow depths G_0 remains mostly below 50 kPa, which is a typical value for clays and sands of low density (Anderson and Stokoe, 1978). The small shear modulus indicates a low shear strength/internal friction angle (residual friction angles are approximately 17 to 18 degrees at 0.5 m bgl; Merritt et al. 2013). Thus small elevations in pore pressures can decrease the effective stress at critical slip surfaces to such an extent that landslide reactivation occurs despite a shallow slope angle of only 14° (Uhlemann et al., 2016). The rapidly increasing values of G_0 at depths > 5 m bgl indicate that the majority of slope failures will occur above this depth, and hence deep-seated failures are unlikely.

Comparing the two moduli suggests that the weathering effect is not registered very clearly by the Young's modulus; it shows values below 350 kPa only to about 2 m bgl. These are characteristic values for very soft to soft clays with high plasticity (Kézdi and Réthâti, 1974). The same soil classification was drawn from laboratory testing of samples of the WMF (Hobbs et al., 2012). With values of up to 5 MPa, the Young's modulus of deeper layers takes values characteristic of soft to firm clay and silt, and loose sands (Look, 2007). Examination of borehole logs obtained from shallow boreholes (< 6 m) revealed a similar lithology and soil strength (Gunn et al., 2013) of material representative for both WMF and SSF. A previous study employing cone penetration tests (CPT) investigated the soil properties of the shallow material (< 4 m) of the lobes (Gunn et al., 2013). While this formed a smaller and shallower investigation than was performed in the seismic study, it forms an intrusive data set for comparison with the shear and Young's modulus derived from the seismic data, between which commonly a linear relationship exist (Robertson, 2009). The agreement between the CPT results (Fig. 8a) and the Young's modulus derived from the P- and S-wave SRT is very good (Fig. 6), both in the magnitude and spatial correlation. Generally, the upper 0.5 m show considerably smaller values than observed from the seismic data. This is most likely be caused by the limited sensitivity of the seismic techniques within this layer. Both, CPT and SRT derived Young's moduli show smaller values below the front of the lobe, between y = 33 m and 44 m. This is an indication of a lower moisture content in this area (Gregory, 1976), but could also suggest a lower local stress field and increased weathering/fabric dilation (Macari and Laureano, 1996). Direct comparison of SRT derived Young's moduli with cone resistance at the CPT locations (Fig. 8b and c) highlights this linear relationship between the two properties. The very good correlation between SRT and intrusive investigation (Pearson's r = 0.93 and 0.81 for locations CPT2 and CPT4, respectively) underlines their complementary nature.

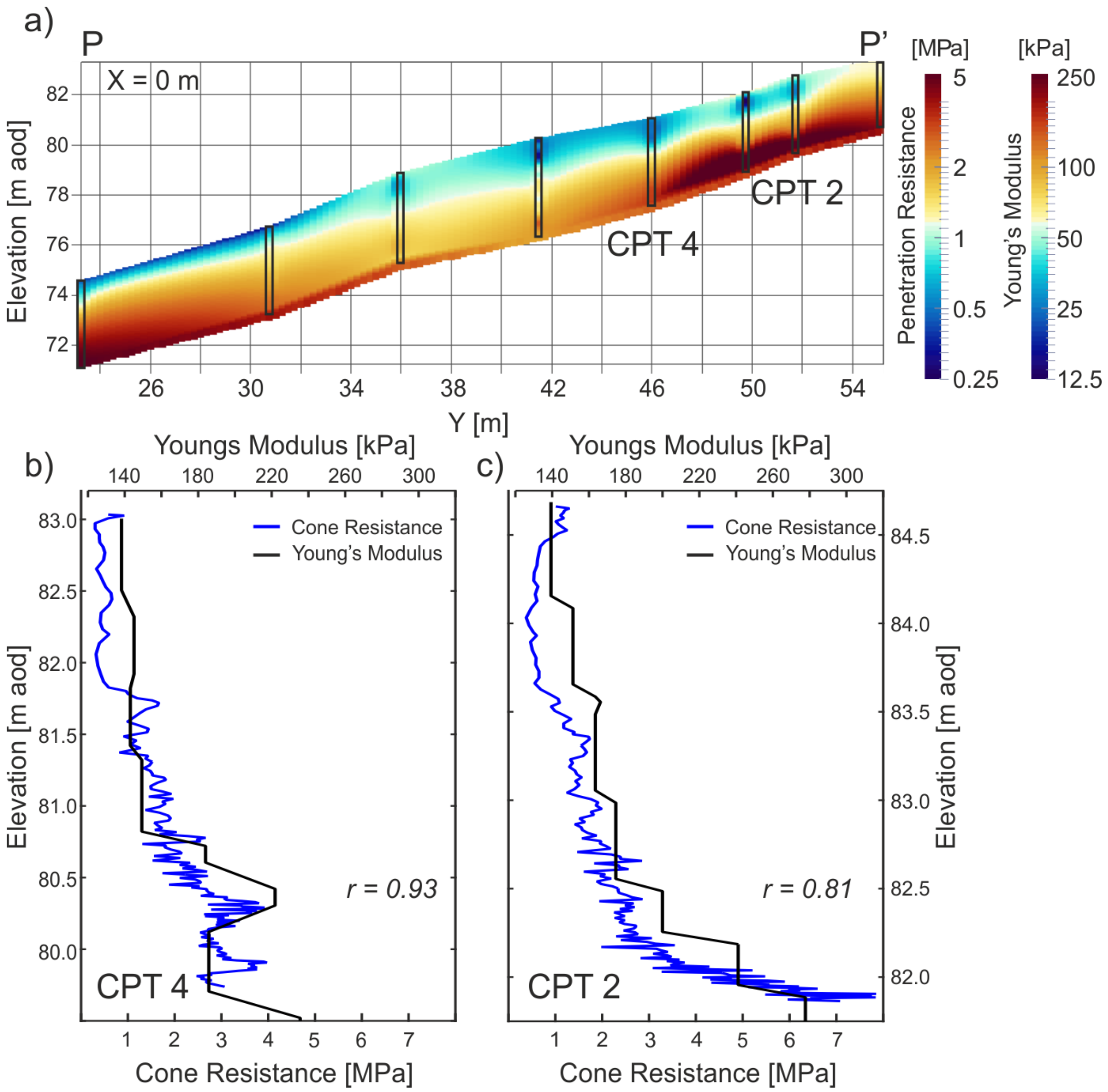

Fig. 8 a) Cross-section of penetration resistance, acquired along a 36 m long stretch next to L1 (see Fig. 1 and Fig. 5; modified from Gunn et al. (2013)*). The area between test locations (black rectangles) was interpolated using an inverse distance weighting approach. The scale for the Young's modulus was derived from the cone resistance using a simplified linear relationship* (Robertson, 2009)*. b) and c) intrusive cone resistance and SRT derived Young's modulus at CPT locations CPT 2 and 4. Note the very good correlation between the two methods.*

4.3 Poisson's ratio

For the interpretation of the Poisson's ratio we define a threshold of v = 0.4, above which material can be classified as saturated clay or sand, while below this threshold the material is more likely to comprise partially saturated sand or silt (Bowles, 1988; Gercek, 2007). Applying this and comparing the imaged Poisson's ratio with the geological understanding of the site (Fig. 1c), a strong correlation can be observed. While $v > 0.4$ in the translation-dominant domain coincides with the assumed location of the WMF, $v < 0.4$ is found in the location of the SSF and DF. The layer of $v > 0.4$ underlying the central part of the slope indicates an increase in moisture content and perhaps porosity (Gregory, 1976; Pasquet et al., 2015). It is likely to represent the saturated state of the SSF, with its upper boundary representing the regional groundwater table. This is consistent with the observations from the P-wave velocity profiles (Fig. 5c) and field observations. The decreasing values at the southern-most part of the survey area may indicate the distribution of the RMF.

Electrical resistivity tomography (ERT) data was acquired during the time of the SRT survey using a permanently installed monitoring system (Wilkinson et al., 2010, 2016). Both SRT derived Poisson's ratio and ERT data are sensitive to variations in moisture content. Assuming that the electrical conductivity of the pore fluid is constant over the imaging volume, moisture content can be derived from ERT data provided a property relationship between moisture content and resistivity is known (for details on data acquisition and processing see Chambers et al., 2011, and Wilkinson et al., 2016; for details on translation of resistivity to gravimetric moisture content see Chambers et al., 2014, Gunn et al., 2014, and Merritt et al., 2016). Comparing the ERT derived moisture content (iso-volumes in Fig. 9) with the Poisson's ratio shows a good correlation (Pearson's $r = 0.53$). Note the excellent agreement showing high moisture content and Poisson's ratio of the WMF sliding over the SSF at the top of the eastern lobe at $x = 40$ m and $y > 60$ m. Also the central part of the SSF (x = 20 m, y < 60 m) is shown to be of low moisture content and Poisson's ratio. Thus, a P- and S-wave derived Poisson's ratio can be used to assess the moisture content of these formations.

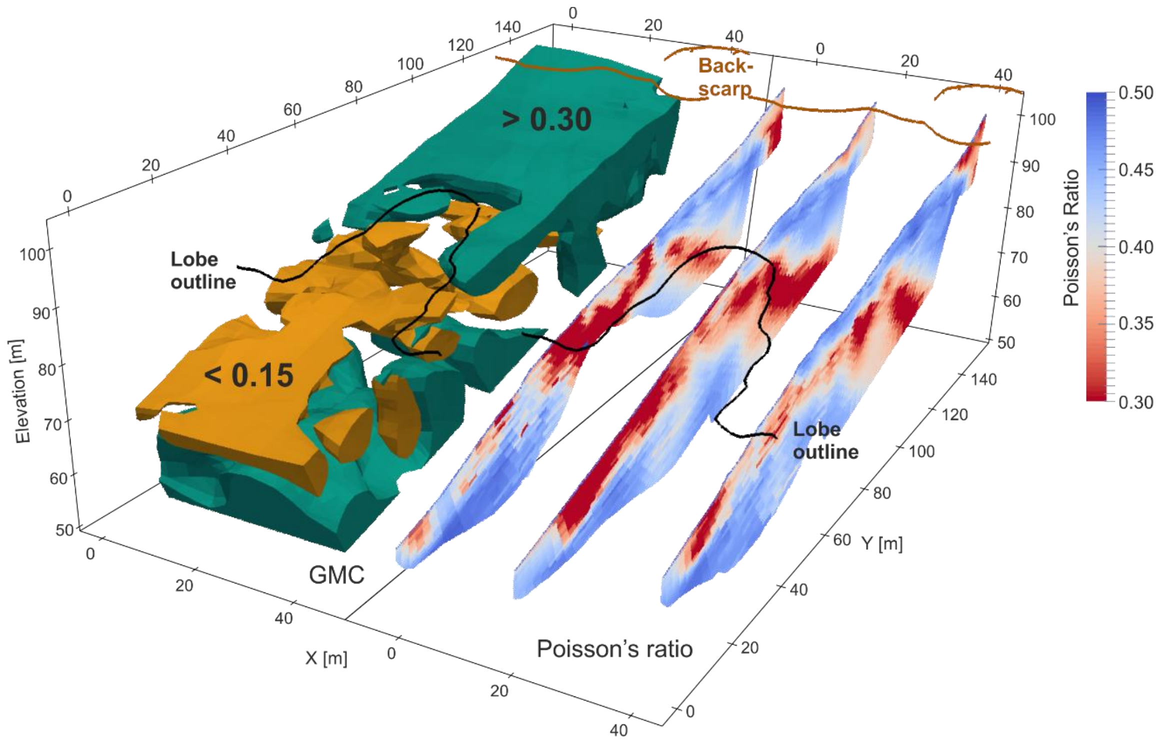

Fig. 9 Iso-volumes of ERT derived gravimetric moisture content (GMC) and SRT derived Poisson's ratios of profiles L1-L3 (cross-sections). Shown are values of GMC > 0.30 (turquois) and GMC < 0.15 (orange).

At L2, located between the two studied lobes, the low Poisson's ratios of the SSF are very pronounced and show a clear distinction to the WMF and the underlying higher values of *v*. A higher degree of distortion, resulting in higher Poisson's ratios, can be observed along the lobes of L1, L3, and L4, indicating higher moisture content than observed in the central part of the slope. This may support the hypothesis that mass movements of the flow lobes are controlled by base drainage at the sliding surface (Uhlemann et al., 2016).

4.4 Landslide characteristics

The landslide characteristics can be derived from a joint interpretation of the P- and S-wave velocity, elastic moduli, and Poisson's ratio distributions. The landslide consists, in general, of three types of materials, (1) saturated clay of the WMF overlying (2) partially saturated sandy silts and clayey silts and (3) saturated sandy silts and clayey silts of the SSF (Fig. 10). Next to the lithology, the degree of saturation/material density is a crucial input parameter for landslide modelling, as it provides indications of which geotechnical properties may be most appropriate to underpin the reconstruction of mass movement processes and support the numerical analysis of slope stability (e.g., drained or undrained shear strength).

In the translation-dominant domain, a continuous surface zone of deforming deposits is observed (Fig. 10) but with different relative densities. It is thought that these may relate to a wave of deformation progressing through the slope at the time of observation. The darker shades represent material that is likely under tension while the light-grey represents denser material that is likely undergoing a phase of compression in the cascade of accumulating strains that progress downslope. The lower part of the 'tension' zone extends into the top of the flow-dominant domain where deformation is most likely controlled by undrained shear strength with transitions towards viscous deformation. As deformation progresses, drainage of the reworked material is thought to take place along the base of the flow lobes, leading to a gradual mobilisation of frictional resistance and resulting in stabilisation of the mass movement even though the local slope becomes steeper.

Reactivation of landslide activity is a function of wetting up of the landslide body, predominantly through direct infiltration following periods of prolonged/intense rainfall, further assisted by groundwater inflow from the DF. During relatively dry periods comparably slow deformations (< 15 cm/year) within the lobes can be observed, and these are likely the local adjustments in strain to even out imbalances in the tension-compression stress field in the translation-dominant domain.

The critical stiffness threshold (CST, v_p = 800 m/s) shows significant variation throughout the slope. It is found between 2 m and 5 m bgl in the lower and upper parts, although increasing in depth towards the northern boundary (profile distance > 135 m) of the study area. In the central part it reaches depths of up to 17 m bgl. This could be a reflection of an enhanced susceptibility of a local lithology to weathering and de-structuring. It is potentially possible that this boundary reflects palaeo-mass movements, but this is not evident from existing borehole records (Uhlemann et al., 2016). Note that P-wave velocities, on which the CST is based on, vary with saturation. Thus, its shallower depth at y > 100 m could also be caused by a perched water table.

Under the current hydrological situation episodic deformation along a pre-existing slip surfaces predominantly caused by prolonged rainfall define the landslide behaviour. If drainage pathways close or reduce in the future, this may change and the risk of a comparably deep-seated failure should be reassessed.

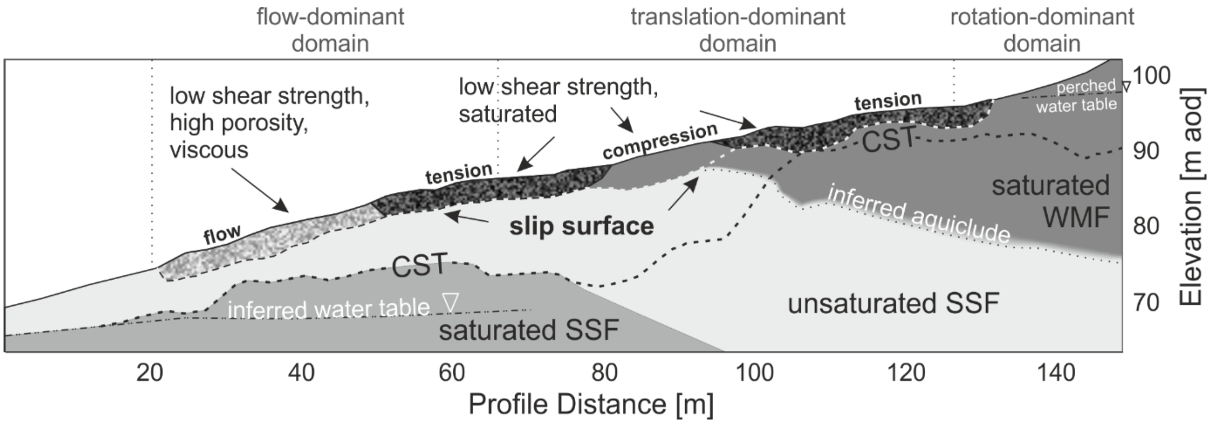

Fig. 10 Schematic ground model of the landslide, derived from the P- and S-wave SRT, elastic moduli, and Poisson's ratio distributions. The critical stiffness threshold (CST) indicates the perceived maximum depth of weathering and de-structuring.

5. Conclusions

Site investigations are usually limited to surface observations, borehole or intrusive investigation, and laboratory measurements, providing surficial or information at depth profile or samples of discrete points only. In the case of landslide studies, where ground heterogeneities in both material and hydrological properties may define the failure mechanism and trigger, this is often not appropriate. The approach presented here overcomes this by employing P- and S-wave SRT, and deriving distributions of elastic moduli and the Poisson's ratio from this data. The main benefit of this study, and the information obtained from the Poisson's ratio in particular, is the spatial information relating to saturation state and potential strength of the ground. This information is crucial for an accurate definition of landslide models.

The P- and S-wave SRT indicated very low velocities of v_p < 500 m/s and v_s < 150 m/s in the depths above 5 m bgl. These could be related to a high degree of weathering, de-stressing and de-structuring, with high porosity and low density. P-wave velocities of v_p > 1500 m/s close to the toe of the slope were assigned to the regional groundwater table. Despite these features, v_p and v_s failed to provide an indication of the different lithological units present at site. These were only imaged by deriving the Poisson's ratio from the velocity distributions. The saturated clays of the WMF showed Poisson's ratios $v > 0.4$, while the partially saturated sandy silts and clayey silts of the SSF showed $v < 0.4$. Both shear and Young's modulus, also derived from the seismic velocity distributions, showed small values ($G_0 < 1.0$ MPa, $E < 5$ MPa) throughout the slope, indicating the small strength of the material constituting the slope. Minima of the elastic moduli were found at the actively moving parts of the landslide, highlighting the reduced strength of the material leading to mass movements at shallow slope angles. An interpretation of the mechanical properties derived from this study concluded that deep-seated failures are unlikely, and occasional reactivation of landslide movements in response to prolonged intense rainfall is the main failure mechanism.

It is difficult to directly compare material properties derived from field measurements and from laboratory studies. Collecting truly undisturbed samples from the field is fraught with difficulty and reconstructing the in situ stress field is very challenging. In addition, very small strain characterisation of soft sediments and soils is very difficult using conventional laboratory assessments (that are better at characterisation of intermediate to large strains). Further work is needed to investigate the relationships in order to successfully combine the two approaches (e.g. Mavko et al., 2009; Zhang et al., 2009).

This methodology has the potential to provide the spatial distribution of elastic moduli and Poisson's ratio forming a major improvement upon the discrete sampling/testing programmes of standard site investigations where large slopes are characterised by often very sparse data. The introduction of spatially varying parameters in a 2/3D environment enables construction of detailed ground models that form a step change in the analysis of landslide failure mechanisms and movement. In turn, a better suite of tools to interpret landslide behaviour in greater detail will significantly contribute to more appropriate management practices and disaster risk reduction strategies, particularly where the landslide hazard affects vulnerable infrastructure and communities (Dijkstra and Dixon, 2010; Dijkstra et al., 2014; Glendinning et al., 2015; Longoni et al., 2016).

6. Acknowledgements

We would like to convey our gratitude to Steve and Josie Gibson (the landowners of Hollin Hill) for the continuous support and involvement in the research conducted at the landslide observatory. We thank the editor and two anonymous reviewers for their constructive comments. The Natural Environment Research Council (NERC) supported this research. This paper is published with the permission of the Executive Director of the British Geological Survey (NERC).

References

Anderson, D.G., Stokoe, K.H., 1978. Shear modulus: a time-dependent soil property. Dyn. Geotech. Testing, ASTM SPT 654, 66–90.

Atkinson, J.H., 2000. Non-linear soil stiffness in routine design. Géotechnique 50, 487–508. doi:10.1680/geot.2000.50.5.487

Benz, T., 2007. Small-Strain Stiffness of Soils and its Numerical Consequences. University of Stuttgart.

Biot, M.A., 1941. General Theory of Three-Dimensional Consolidation. J. Appl. Phys. 12, 155. doi:10.1063/1.1712886

Bird, J.F., Bommer, J.J., 2004. Earthquake losses due to ground failure. Eng. Geol. 75, 147–179. doi:10.1016/j.enggeo.2004.05.006

Bowles, J.E., 1988. Foundation analysis and design, Engineering Geology. McGraw-Hill Companies, Inc., Singapore.

BSI, 2015. BS 5930:2015 Code of practice for ground investigations.

Caris, J.P.T., Van Asch, T.W.J., 1991. Geophysical, geotechnical and hydrological investigations of a small landslide in the French Alps. Eng. Geol. 31, 249–276. doi:10.1016/0013-7952(1)90011-9

Cascini, L., Ciurleo, M., Di Nocera, S., Gullà, G., 2015. A new–old approach for shallow landslide analysis and susceptibility zoning in fine-grained weathered soils of southern Italy. Geomorphology 241, 371–381. doi:10.1016/j.geomorph.2015.04.017

Chambers, J.E., Gunn, D.A., Wilkinson, P.B., Meldrum, P.I., Haslam, E., Holyoake, S., Kirkham, M., Kuras, O., Merritt, A., Wragg, J., 2014. 4D electrical resistivity tomography monitoring of soil moisture dynamics in an operational railway embankment. Near Surf. Geophys. 12, 61–72. doi:10.3997/1873-0604.2013002

Chambers, J.E., Wilkinson, P.B., Kuras, O., Ford, J.R., Gunn, D.A., Meldrum, P.I., Pennington, C.V.L., Weller, A.L., Hobbs, P.R.N., Ogilvy, R.D., 2011. Three-dimensional geophysical anatomy of an active landslide in Lias Group mudrocks, Cleveland Basin, UK. Geomorphology 125, 472–484. doi:10.1016/j.geomorph.2010.09.017

Clayton, C.R.I., 2011. Stiffness at small strain: research and practice. Géotechnique 61, 5–37. doi:10.1680/geot.2011.61.1.5

Crozier, M.J., Glade, T., 2005. Landslide Hazard and Risk: Issues, Concepts and Approach, in: Glade, T., Anderson, M., Crozier, M.J. (Eds.), Landslide Hazard and Risk. John Wiley & Sons, Ltd, Chichester, West Sussex, England, pp. 1–40. doi:10.1002/9780470012659

Cruden, D.M., Varnes, D.J., 1996. Landslide types and processes. Turn. AK, Schuster, RL Landslides Investig. mitigation, Spec. Rep. 247. 36–75.

Das, B.M., 2008. Advanced Soil Mechanics, Third Edit. ed. Taylor & Francis, New York.

Davidovici, V., 1985. Génie parasismique. École Nationale des Ponts et Chaussées, Paris.

Dijkstra, T. a., Dixon, N., 2010. Climate change and slope stability in the UK: challenges and approaches. Q. J. Eng. Geol. Hydrogeol. 43, 371–385. doi:10.1144/1470-9236/09-036

Dijkstra, T., Dixon, N., Crosby, C., Frost, M., Gunn, D., Fleming, P., Wilks, J., Uk, C., 2014. Forecasting infrastructure resilience to climate change. Proc. Inst. Civ. Eng. 167, 269–280. doi:http://dx.doi.org/10.1680/tran.13.00089

Dixon, N., Spriggs, M.P., Smith, A., Meldrum, P., Haslam, E., 2014. Quantification of reactivated landslide behaviour using acoustic emission monitoring. Landslides 12, 549–560. doi:10.1007/s10346-014-0491-z

Donohue, S., Long, M., O'Connor, P., Eide Helle, T., Pfaffhuber, A.A., Rømoen, M., 2012. Multi-method geophysical mapping of quick clay. Near Surf. Geophys. 10, 207–219. doi:10.3997/1873-0604.2012003

Gaunt, G.D., Ivimey-Cook, H.C., Penn, I.E., Cox, B.M., 1980. Mesozoic Rocks Proved by IGS Boreholes in the Humber and Acklam Areas. Institute of Geological Studies, Nottingham.

Gercek, H., 2007. Poisson's ratio values for rocks. Int. J. Rock Mech. Min. Sci. 44, 1–13. doi:10.1016/j.ijrmms.2006.04.011

Giannakopoulos, A.E., Suresh, S., 1997. Indentation of solids with gradients in elastic properties: Part II. axisymmetric indentors. Int. J. Solids Struct. 34, 2393–2428. doi:10.1016/S0020-7683(96)00172-2

Glendinning, S., Helm, P.R., Rouainia, M., Stirling, R.A., Asquith, J.D., Hughes, P.N., Toll, D.G., Clarke, D., Powrie, W., Smethurst, J., Hughes, D., Harley, R., Karim, R., Dixon, N., Crosby, C., Chambers, J., Dijkstra, T., Gunn, D., Briggs, K., Muddle, D., 2015. Research-informed design, management and maintenance of infrastructure slopes: development of a multi-scalar approach. IOP Conf. Ser. Earth Environ. Sci. 26, 012005. doi:10.1088/1755-1315/26/1/012005

Glendinning, S., Hughes, P., Helm, P., Chambers, J., Mendes, J., Gunn, D., Wilkinson, P., Uhlemann, S., 2014. Construction, management and maintenance of embankments used for road and rail infrastructure: implications of weather induced pore water pressures. Acta Geotech. 9, 799–816. doi:10.1007/s11440-014-0324-1

Grandjean, G., Hibert, C., Mathieu, F., Garel, E., Malet, J.-P., 2009. Monitoring water flow in a clay-shale hillslope from geophysical data fusion based on a fuzzy logic approach. Comptes Rendus Geosci. 341, 937–948.

Gregory, A.R., 1976. Fluid Saturation Effects on Dynamic Elastic Properties of Sedimentary Rocks. Geophysics 41, 895–921.

Grelle, G., Guadagno, F.M., 2009. Seismic refraction methodology for groundwater level determination: "Water seismic index." J. Appl. Geophys. 68, 301–320. doi:10.1016/j.jappgeo.2009.02.001

Griffiths, D. V., Lane, P.A., 1999. Slope stability analysis by finite elements. Geotechnique 49, 387–403.

Guadalupe, Y., Baxter, C., Sharma, M., 2013. Measuring Shear Wave Velocity in Laboratory to Link Small- and Large-Strain Behavior of Soils. Transp. Res. Rec. J. Transp. Res. Board 2335, 79–88. doi:10.3141/2335-09

Gunn, D.A., Chambers, J.E., Hobbs, P.R.N., Ford, J.R., Wilkinson, P.B., Jenkins, G.O., Merritt, A., 2013. Rapid observations to guide the design of systems for long-term monitoring of a complex landslide in the Upper Lias clays of North Yorkshire, UK. Q. J. Eng. Geol. Hydrogeol. 46, 323–336. doi:10.1144/qjegh2011-028

Gunn, D.A., Chambers, J.E., Uhlemann, S., Wilkinson, P.B., Meldrum, P.I., Dijkstra, T.A., Haslam, E., Kirkham, M., Wragg, J., Holyoake, S., Hughes, P.N., Hen-Jones, R., Glendinning, S., 2014. Moisture monitoring in clay embankments using electrical resistivity tomography. Constr. Build. Mater. 92, 82–94. doi:10.1016/j.conbuildmat.2014.06.007

Heincke, B., Maurer, H., Green, A.G., Willenberg, H., Spillmann, T., Burlini, L., 2006. Characterizing an unstable mountain slope using shallow 2D and 3D seismic tomography. Geophysics 71, B241–B256. doi:10.1190/1.2338823

Hibert, C., Grandjean, G., Bitri, A., Travelletti, J., Malet, J.-P., 2012. Characterizing landslides through geophysical data fusion: Example of the La Valette landslide (France). Eng. Geol. 128, 23–29.

Hobbs, P.R.N., Entwisle, D.C., Northmore, K.J., Sumbler, M.G., Jones, L.D., Kemp, S., Self, S., Barron, M., Meakin, J.L., 2012. Engineering geology of British rocks and soils: Lias Group (No. OR/12/032).

Huang, A.-B., Lee, J.-T., Ho, Y.-T., Chiu, Y.-F., Cheng, S.-Y., 2012. Stability monitoring of rainfall-induced deep landslides through pore pressure profile measurements. Soils Found. 52, 737–747. doi:10.1016/j.sandf.2012.07.013

Hungr, O., Leroueil, S., Picarelli, L., 2014. The Varnes classification of landslide types, an update. Landslides. doi:10.1007/s10346-013-0436-y

Jongmans, D., Bièvre, G., Renalier, F., Schwartz, S., Beaurez, N., Orengo, Y., 2009. Geophysical investigation of a large landslide in glaciolacustrine clays in the Trièves area (French Alps). Eng. Geol. 109, 45–56. doi:10.1016/j.enggeo.2008.10.005

Jongmans, D., Garambois, S., 2007. Geophysical investigation of landslides: a review. Bull. la Société géologique Fr. 33, 101–112.

Kézdi, Á., Rétháti, L., 1974. Handbook of soil mechanics. Elsevier, Amsterdam.

Lacasse, S., Nadim, F., 2009. Landslide Risk Assessment and Mitigation Strategy, in: Sassa, K., Canuti, P. (Eds.), Landslides – Disaster Risk Reduction. Springer Berlin Heidelberg, Berlin, Heidelberg, pp. 31–61.

Lacroix, P., Amitrano, D., 2013. Long-term dynamics of rockslides and damage propagation inferred from mechanical modeling. J. Geophys. Res. Earth Surf. 118, 2292–2307.

doi:10.1002/2013JF002766

Lanz, E., Maurer, H., Green, A.G., 1998. Refraction tomography over a buried waste disposal site. GEOPHYSICS 63, 1414–1433. doi:10.1190/1.1444443

Leroueil, S., 2001. Natural slopes and cuts: movement and failure mechanisms. Géotechnique 51, 197–243. doi:10.1680/geot.2001.51.3.197

Lissak, C., Maquaire, O., Malet, J.P., Bitri, A., Samyn, K., Grandjean, G., Bourdeau, C., Reiffsteck, P., Davidson, R., 2014. Airborne and ground-based data sources for characterizing the morpho-structure of a coastal landslide. Geomorphology 217, 140–151. doi:10.1016/j.geomorph.2014.04.019

Longoni, L., Papini, M., Brambilla, D., Arosio, D., Zanzi, L., 2016. The role of the spatial scale and data accuracy on deep-seated gravitational slope deformation modeling: The Ronco landslide, Italy. Geomorphology 253, 74–82. doi:10.1016/j.geomorph.2015.09.030

Look, B., 2007. Handbook of Geotechnical Investigation and Design Tables. Taylor & Francis, London, UK.

Macari, E.J., Laureano, H., 1996. Effect of Degree of Weathering on Dynamic Properties of Residual Soils. J. Geotech. Eng. 122, 988–997.

Martel, S.J., Muller, J.R., 2000. A Two-dimensional Boundary Element Method for Calculating Elastic Gravitational Stresses in Slopes. Pure Appl. Geophys. 157, 989–1007. doi:10.1007/s000240050014

Mavko, G., Mukerji, T., Dvorkin, J., 2009. The Rock Physics Handbook. Cambridge University Press, Cambridge. doi:10.1017/CBO9780511626753

Merritt, A.J., Chambers, J.E., Murphy, W., Wilkinson, P.B., West, L.J., Gunn, D. a., Meldrum, P.I., Kirkham, M., Dixon, N., 2013. 3D ground model development for an active landslide in Lias mudrocks using geophysical, remote sensing and geotechnical methods. Landslides 11, 537–550. doi:10.1007/s10346-013-0409-1

Merritt, A.J., Chambers, J.E., Wilkinson, P.B., West, L.J., Murphy, W., Gunn, D., Uhlemann, S., 2016. Measurement and modelling of moisture—electrical resistivity relationship of fine-grained unsaturated soils and electrical anisotropy. J. Appl. Geophys. 124, 155–165. doi:10.1016/j.jappgeo.2015.11.005

Mondol, N.H., Bjørlykke, K., Jahren, J., Høeg, K., 2007. Experimental mechanical compaction of clay mineral aggregates-Changes in physical properties of mudstones during burial. Mar. Pet. Geol. 24, 289–311. doi:10.1016/j.marpetgeo.2007.03.006

Nadim, F., Jaedicke, C., Smebye, H., Kalsnes, B., 2013. Assessment of Global Landslide Hazard Hotspots, in: Landslides: Global Risk Preparedness. Springer Berlin Heidelberg, Berlin, Heidelberg, pp. 59–71. doi:10.1007/978-3-642-22087-6_4

Ohta, Y., Goto, N., 1978. Empirical shear wave velocity equations in terms of characteristic soil indexes. Earthq. Eng. Struct. Dyn. 6, 167–187. doi:10.1002/eqe.4290060205

Paice, G.M., Griffiths, D. V., Fenton, G.A., 1996. Finite Element Modeling of Settlements on Spatially Random Soil. J. Geotech. Eng. 122, 777–779. doi:10.1061/(ASCE)0733-9410(1996)122:9(777)

Pasquet, S., Bodet, L., Dhemaied, A., Mouhri, A., Vitale, Q., Rejiba, F., Flipo, N., Guérin, R., 2015. Detecting different water table levels in a shallow aquifer with combined P-, surface and SH-wave surveys: Insights from VP/VS or Poisson’s ratios. J. Appl. Geophys. 113, 38–50. doi:10.1016/j.jappgeo.2014.12.005

Perrone, A., Lapenna, V., Piscitelli, S., 2014. Electrical resistivity tomography technique for landslide investigation: A review. Earth-Science Rev. 135, 65–82. doi:10.1016/j.earscirev.2014.04.002

Petley, D., 2013. Global losses from landslides associated with dams and reservoirs. Ital. J. Eng. Geol. Environ. 63–72. doi:10.4408/IJEGE.2013-06.B-05

Petley, D., 2012. Global patterns of loss of life from landslides. Geology 40, 927–930. doi:10.1130/G33217.1

Podvin, P., Lecomte, I., 1991. Finite difference computation of traveltimes in very contrasted velocity models: a massively parallel approach and its associated tools. Geophys. J. Int. 105, 271–284. doi:10.1111/j.1365-246X.1991.tb03461.x

Popescu, M.E., Sasahara, K., 2009. Engineering Measures for Landslide Disaster Mitigation, in: Sassa, K., Canuti, P. (Eds.), Landslides – Disaster Risk Reduction. Springer Berlin Heidelberg, Berlin, Heidelberg, pp. 609–631. doi:10.1007/978-3-540-69970-5

Robertson, P.K., 2009. Interpretation of cone penetration tests — a unified approach. Can. Geotech. J. 46, 1337–1355. doi:10.1139/T09-065

Salas-Romero, S., Malehmir, A., Snowball, I., Lougheed, B.C., Hellqvist, M., 2015. Identifying landslide preconditions in Swedish quick clays—insights from integration of surface geophysical, core sample- and downhole property measurements. Landslides. doi:10.1007/s10346-015-0633-y

Sass, O., Bell, R., Glade, T., 2008. Comparison of GPR, 2D-resistivity and traditional techniques for the subsurface exploration of the ??schingen landslide, Swabian Alb (Germany). Geomorphology 93, 89–103. doi:10.1016/j.geomorph.2006.12.019

Schaetzl, R.J., Anderson, S., 2005. Soils: Genesis and Geomorphology, 6th ed. Cambridge University Press, Cambridge, UK.

Schrott, L., Sass, O., 2008. Application of field geophysics in geomorphology: Advances and limitations exemplified by case studies. Geomorphology 93, 55–73. doi:10.1016/j.geomorph.2006.12.024

Smith, A., Dixon, N., 2015. Quantification of landslide velocity from active waveguide–generated acoustic emission. Can. Geotech. J. 52, 413–425. doi:10.1139/cgj-2014-0226

Smith, A., Dixon, N., Meldrum, P., Haslam, E., Chambers, J., 2014. Acoustic emission monitoring of a soil slope : Comparisons with continuous deformation measurements. Geotech. Lett. 4, 255–261. doi:http://dx.doi.org/10.1680/geolett.14.00053

Springman, S.M.M., Kienzler, P., Friedel, S., Thielen, a., Kienzler, P., Friedel, S., 2013. A long-term field study for the investigation of rainfall-induced landslides. Geotechnique 63, 1177–1193. doi:10.1680/geot.11.P.142

Telford, W.M., Geldart, L.P., Sheriff, R.E., 1990. Applied geophysics, Second Edi. ed. Cambridge University Press, Cambridge, UK.

Turesson, A., 2007. A comparison of methods for the analysis of compressional, shear, and surface wave seismic data, and determination of the shear modulus. J. Appl. Geophys. 61, 83–91. doi:10.1016/j.jappgeo.2006.04.005

Uhlemann, S., Smith, A., Chambers, J., Dixon, N., Dijkstra, T., Haslam, E., Meldrum, P., Merritt, A., Gunn, D., Mackay, J., 2016. Assessment of ground-based monitoring techniques applied to landslide investigations. Geomorphology 253, 438–451. doi:10.1016/j.geomorph.2015.10.027

Uhlemann, S., Wilkinson, P.B., Chambers, J.E., Maurer, H., Merritt, A.J., Gunn, D.A., Meldrum, P.I., 2015. Interpolation of landslide movements to improve the accuracy of 4D geoelectrical monitoring. J. Appl. Geophys. 121, 93–105. doi:10.1016/j.jappgeo.2015.07.003

Van Dam, R.L., 2012. Landform characterization using geophysics-Recent advances, applications, and emerging tools. Geomorphology 137, 57–73. doi:10.1016/j.geomorph.2010.09.005

van Westen, C.J., van Asch, T.W.J., Soeters, R., 2006. Landslide hazard and risk zonation—why is it still so difficult? Bull. Eng. Geol. Environ. 65, 167–184. doi:10.1007/s10064-005-0023-0

Wilkinson, P., Chambers, J., Uhlemann, S., Meldrum, P., Smith, A., Dixon, N., Loke, M.H., 2016. Reconstruction of landslide movements by inversion of 4D electrical resistivity tomography monitoring data. Geophys. Res. Lett. doi:10.1002/2015GL067494

Wilkinson, P.B., Chambers, J.E., Meldrum, P.I., Gunn, D.A., Ogilvy, R.D., Kuras, O., 2010. Predicting the movements of permanently installed electrodes on an active landslide using time-lapse geoelectrical resistivity data only. Geophys. J. Int. 183, 543–556. doi:10.1111/j.1365-246X.2010.04760.x

Xia, J., Miller, R.D., Park, C.B., Wightman, E., Nigbor, R., 2002. A pitfall in shallow shear-wave refraction surveying. J. Appl. Geophys. 51, 1–9. doi:10.1016/S0926-9851(02)00197-0

Yamakawa, Y., Kosugi, K., Masaoka, N., Sumida, J., Tani, M., Mizuyama, T., 2012. Combined geophysical methods for detecting soil thickness distribution on a weathered granitic hillslope. Geomorphology 145-146, 56–69. doi:10.1016/j.geomorph.2011.12.035

Yilmaz, Ö., 2015. 1. Seismic Waves, in: Engineering Seismology with Applications to Geotechnical Engineering. Society of Exploration Geophysicists, pp. 27–157. doi:10.1190/1.9781560803300.ch1

Zhang, J., Lang, J., Standifird, W., 2009. Stress, porosity, and failure-dependent compressional and shear velocity ratio and its application to wellbore stability. J. Pet. Sci. Eng. 69, 193–202. doi:10.1016/j.petrol.2009.08.012